IOP Publishing Journal of Physics D: Applied Physics
J. Phys. D: Appl. Phys. **40** (2007) 2961–2971 doi:10.1088/0022-3727/40/9/044

Lattice Boltzmann method for continuum, multi-component mass diffusion in complex 2D geometries

Abhijit S Joshi, Aldo A Peracchio, Kyle N Grew and Wilson K S Chiu[1]

Department of Mechanical Engineering, The University of Connecticut, 191 Auditorium Road, Storrs, CT 06269-3139, USA

E-mail: wchiu@engr.uconn.edu

Received 15 May 2006, in final form 4 December 2006
Published 19 April 2007
Online at stacks.iop.org/JPhysD/40/2961

Abstract
Multi-component gas diffusion in the continuum flow regime is often modelled using the Stefan–Maxwell (SM) equations. Recent advances in lattice Boltzmann (LB) mass diffusion models have made it possible to directly compare LB predictions with solutions to the SM equations. In this work, one-dimensional (1D) and two-dimensional (2D), equi-molar counter-diffusion of two gases in the presence of a third, inert gas is studied. The work is an extension and validation of a recently proposed binary LB model for components having dissimilar molecular weights. The treatment of inflow and outflow boundary conditions (for specifying species mole fractions or mole flux) is developed via the averaging of component velocities before and after collisions. Results for one and two spatial dimensions have been compared with analytic and numerical solutions to the SM equations and good agreement has been found for a wide range of parameters and for large variations in molecular weights. A novel molecular weight tuning strategy for increasing the accuracy has been demonstrated. The model developed can be used to model continuum, multi-component mass transfer in complex geometries such as porous media without empirical modification of diffusion coefficients based on porosity and tortuosity values. An envisioned application of this technique is to model gas diffusion in porous solid oxide fuel cell electrodes.

(Some figures in this article are in colour only in the electronic version)

1. Introduction

Multi-component mass diffusion through porous media is of importance in many applications including flow of gases in fuel cell electrodes [1], permeation of gases through polymer films used for food packaging [2] and transport of gases through soil [3] to name a few. Modelling of this phenomenon at the continuum level is usually carried out using Fick's law for binary diffusion and via the Stefan–Maxwell (SM) equations for diffusion involving more than two species. Recently, the lattice Boltzmann (LB) method [4] has shown considerable promise in simulating fluid flow and mass diffusion through complex flow passages. The present work examines a recently proposed LB scheme [5] that can simulate mass diffusion in a binary mixture with different molecular weights. This work extends the LB model to three species, develops a suitable and accurate treatment for imposing boundary conditions and validates the LB model with solutions to the SM equations. These validations are performed for two simplified cases: 1D diffusion of three species with no solid obstructions and 2D diffusion of two species in the presence of a square obstacle. While these cases were chosen so that LB solutions could be compared with solutions to the SM equations, the method developed here is quite general and is able to simulate diffusion

[1] Author to whom any correspondence should be addressed.

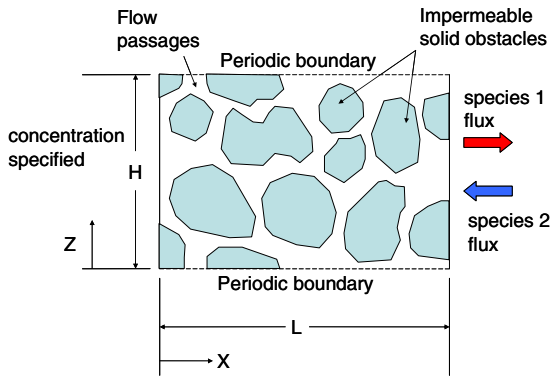

Figure 1. Schematic of mass diffusion through a porous medium.

through a considerably more complex geometry. An extension of the method proposed in this article to three dimensions (3D) is possible but a detailed discussion is beyond the scope of this paper.

The mass diffusion problem considered in this study is illustrated in figure 1 where three species diffuse through a porous medium. On the left boundary ($x = 0$) the total concentration and mole fractions of all three species is specified. On the right boundary ($x = L$) the species mole flux is specified. A special case is considered where the mole flux of species 1 is equal and opposite to that of species 2. The third species is assumed to be inert and thus it has no net mass transfer in or out of the system at steady state. The special case considered here is sometimes referred to as equi-molar counter-diffusion. Periodic boundaries are used at the bottom and top of the domain ($z = 0$ and H, respectively). Several immovable and impermeable solid obstacles can be present in the domain and these allow no mass diffusion (of any species) normal to their surface. In addition, it is assumed that there is no pressure or thermal diffusion and the total concentration of species remains constant throughout the domain. The problem illustrated in figure 1 can be simplified to a 1D problem if all obstacles are removed and there is no variation of species mole fractions at $x = 0$ along the z direction.

The paper is organized as follows. In section 2, the SM equations are introduced and solution procedures for a 1D case without obstacles and a 2D case with a square obstacle are discussed. These solutions are used to validate results from the LB model. A detailed discussion of the LB method is given in section 3. Results are summarized in section 4 and the main conclusions that emerged from this study are presented in section 5.

2. Stefan–Maxwell model

The problem of mass diffusion in a mixture of two species is usually described by Fick's law of diffusion [6] given in equation (1), where $\boldsymbol{J}_i$ is the mole flux of species i, c_T is the total molar concentration, X_i is the mole fraction of species i and D is the diffusion coefficient between the two species.

$$\boldsymbol{J}_i = -c_T D \nabla X_i. \tag{1}$$

Physically, equation (1) states that any species in a mixture will diffuse from regions of higher concentration of that particular species to regions of lower concentration. However, when more than two species are involved, the mass transport becomes more complex and is usually described by the Stefan–Maxwell (SM) equations. The SM equations for an ideal gas mixture consisting of N species are given by [6]

$$-\nabla X_i = \sum_{\substack{j=1 \\ j \neq i}}^{N} \frac{X_j \boldsymbol{J}_i - X_i \boldsymbol{J}_j}{c_T D_{ij}}, \tag{2}$$

where D_{ij} is the mass diffusivity between species i and species j. It can be seen that equation (1) is a special case of equation (2) when $N = 2, \boldsymbol{J}_1 + \boldsymbol{J}_2 = 0$ (equi-molar counter-diffusion) and $D_{12} = D_{21}$.

In general the SM equations are difficult to solve directly as they appear in equation (2). Simplified forms of equation (2) are therefore discussed in what follows as these are amenable to analytical or numerical solution. The first simplified case examined is a 1D case where species 1 and 2 counter diffuse through each other in the presence of a third, inert species. In addition, the counter-diffusion of species 1 and 2 is equi-molar ($J_1 = -J_2 = J$) and along a single spatial direction, x. For this special case, equation (2) simplifies to a set of coupled ordinary differential equations given by

$$\frac{\mathrm{d}X_1}{\mathrm{d}x} = -\left[\frac{X_1 + X_2}{D_{12}} + \frac{X_3}{D_{13}}\right]\frac{J}{c_T}, \tag{3}$$

$$\frac{\mathrm{d}X_2}{\mathrm{d}x} = +\left[\frac{X_1 + X_2}{D_{21}} + \frac{X_3}{D_{23}}\right]\frac{J}{c_T}, \tag{4}$$

$$\frac{\mathrm{d}X_3}{\mathrm{d}x} = X_3\left[\frac{1}{D_{31}} - \frac{1}{D_{32}}\right]\frac{J}{c_T}. \tag{5}$$

Based on specified values of species mole fractions $\{X_1, X_2, X_3\}$ at $x = 0$ and specified mole flux J at $x = L$, equations (3)–(5) can be solved numerically or analytically resulting in mole fraction profiles for all the three species. Note that by reciprocity $D_{12} = D_{21}$, $D_{23} = D_{32}$ and $D_{13} = D_{31}$. These 1D solutions will be used to validate LB model results in section 4.1.

The second simplified case is a 2D case with only two species and with constant diffusivity $D_{12} = D_{21} = D$. If the condition of equi-molar counter-diffusion still holds, the SM equations reduce to Fick's law of diffusion (equation (1)). Invoking the law of conservation of mass, $\nabla \cdot \boldsymbol{J}_i = 0 = -c_T D \nabla^2 X_i$. Thus the mole fraction distribution for any species is governed by the Laplace equation (LE)

$$\nabla^2 X_i = 0. \tag{6}$$

Equation (6) can be solved numerically to obtain mass fraction distributions for a given solution domain and a set of boundary conditions. This 2D solution is compared with LB model results in section 4.2.

3. Lattice Boltzmann model

The LB method used in this work is based on the two-fluid model initially proposed by Luo and Girimaji [7] and extended to components having different molecular weights

by McCracken and Abraham [5]. A detailed discussion and validation of the LB model for binary diffusion can be found in these publications [5, 7] and is not repeated here. This section describes a further extension of the LB model to three components, a novel treatment of inflow and outflow boundary conditions (for specifying mole fraction and mole flux as indicated in figure 1) and further improvement in the numerical stability of the scheme so that species with large differences in molecular weight can be accurately modelled. For completeness, treatment of impermeable obstacles using the bounce-back rule is also discussed.

3.1. Three-species LB model

Unlike conventional computational fluid dynamics (CFD) methods that use fluid density, velocity and pressure as the primary variables, the LB method uses a more fundamental quantity called the particle velocity distribution function (PDF). The PDF f_α^i at any spatial location $\boldsymbol{x}$ and time t is defined as the number of particles of species i travelling with a velocity $\boldsymbol{e}_\alpha^i$ along the direction α. The LB method consists of two basic steps that are carried out at each location (lattice point) on the numerical grid (lattice) covering the solution domain: streaming and collision. Streaming represents movement of particles of each species with a velocity of $\boldsymbol{e}_\alpha^i$ along specified lattice directions α, while collision represents interactions between particles of the same or of different species as they arrive at the lattice point at $\boldsymbol{x}$ from neighbouring points. These steps are combined together in equation (7), the so-called LB equation, written for species i (=1, 2 or 3).

$$f_\alpha^i(\boldsymbol{x} + \boldsymbol{e}_\alpha^i, t + 1) = f_\alpha^i(\boldsymbol{x}, t) + \Omega_\alpha^i(\boldsymbol{x}, t). \tag{7}$$

In equation (7), Ω_α^i represents the collision term, which will be described in detail shortly. For the D2Q9 model [8], the velocity set $\boldsymbol{e}_\alpha^1$ for species 1 (having the least molecular weight) is given by equation (8) and indicated in figure 2(*a*). For a 3D case, it is recommended that the D3Q19 model [8] be adopted but all the derivations in this section are presented for the D2Q9 model.

$$\begin{aligned} &\boldsymbol{e}_0^1 = (0, 0) \qquad \boldsymbol{e}_1^1 = (1, 0) \qquad \boldsymbol{e}_2^1 = (1, 1) \\ &\boldsymbol{e}_3^1 = (0, 1) \qquad \boldsymbol{e}_4^1 = (-1, 1) \qquad \boldsymbol{e}_5^1 = (-1, 0) \\ &\boldsymbol{e}_6^1 = (-1, -1) \qquad \boldsymbol{e}_7^1 = (0, -1) \qquad \boldsymbol{e}_8^1 = (1, -1). \end{aligned} \tag{8}$$

For the remaining species, as per the different lattice speed (DLS) scheme [5], these velocities are obtained using equation (9). The development assumes that diffusion occurs at a constant temperature, and the average kinetic energy of all species is constant. Thus, a heavier species has a lower magnitude of $\boldsymbol{e}_\alpha^i$. It can be assumed without loss of generality that species 1 is the lightest species. The remaining species are ordered such that $M_1 \leqslant M_2$ and $M_1 \leqslant M_3$.

$$\boldsymbol{e}_\alpha^2 = \boldsymbol{e}_\alpha^1 \sqrt{\frac{M_1}{M_2}} \qquad \boldsymbol{e}_\alpha^3 = \boldsymbol{e}_\alpha^1 \sqrt{\frac{M_1}{M_3}}. \tag{9}$$

Note that the lattice in figure 2(*a*) is designed such that node spacing is the same as $\boldsymbol{e}_\alpha^1$, so particles of species 1 stream to neighbouring nodes in a single time-step, while particles of species 2 and 3 stream a shorter distance to off-lattice locations during the same time interval. The streamed values of f_α^2 and f_α^3 at lattice locations are obtained via interpolation. In lieu of the more complex second-order interpolation scheme [5], a simple bi-linear interpolation has been used here for simplicity. Streaming is thus carried out in two steps: in the first step, PDFs for species 1 are streamed from lattice sites to adjacent lattice sites, while PDFs for species 2 and 3 stream from lattice sites to off-lattice sites. In the second step, interpolation is used to determine PDF values for species 2 and 3 at lattice sites. As an

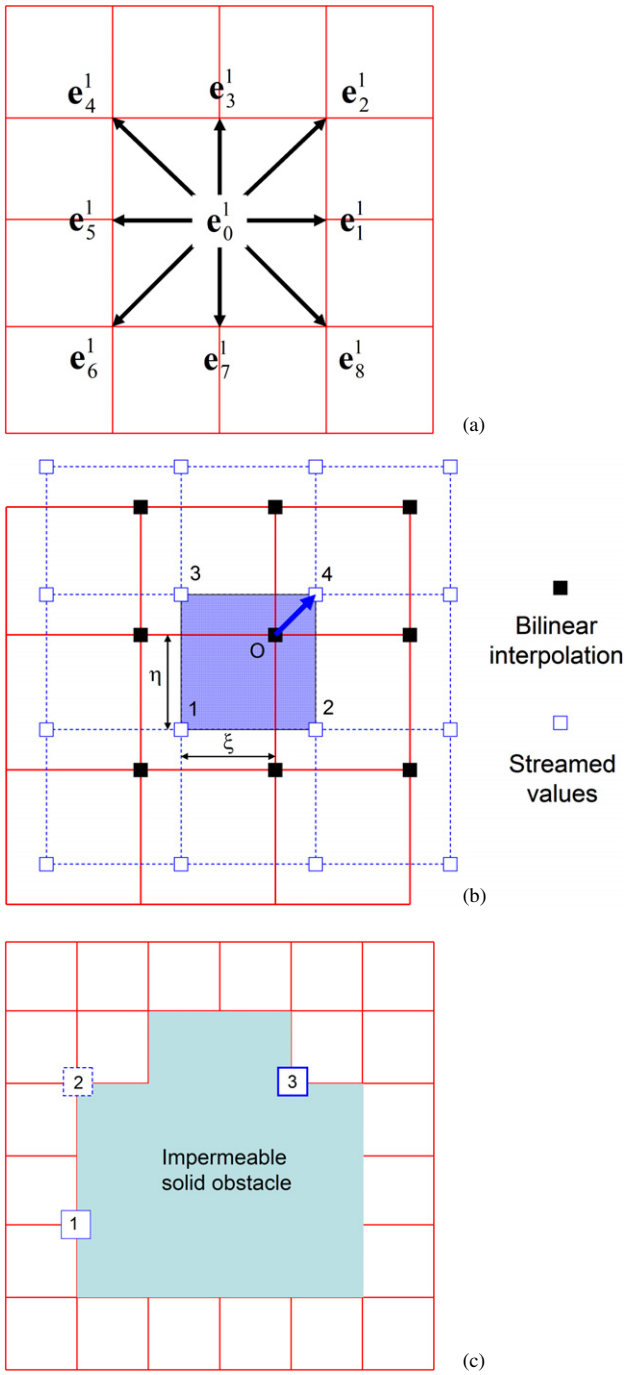

Figure 2. (*a*) D2Q9 velocity model for species 1 (lightest species), (*b*) interpolation scheme for species 2 or 3 for the direction $\alpha = 2$, (*c*) types of lattice points on the obstacle boundary.

example, figure 2(*b*) indicates how the PDF f_α^2 is interpolated at different lattice points. The location of the lattice point (dark square) where interpolation is to be carried out is specified by the fractions ξ and η. The interpolated value F_O at point O in terms of the values F_1, F_2, F_3 and F_4 at the locations indicated in figure 2(*b*) is given by

$$F_O = (1-\xi)(1-\eta)F_1 + \xi(1-\eta)F_2 + (1-\xi)\eta F_3 + \xi\eta F_4. \tag{10}$$

For lattice points on the domain boundaries, or on solid obstacles (figure 2(*c*)), streaming can occur to fictitious points outside the domain or inside solid obstacles in order to interpolate PDF values at the boundary nodes. If the D3Q19 model is adopted for the 3D case, equation (10) can still be used because base velocities in the D3Q19 model are restricted to three mutually perpendicular planes and equation (10) applies for interpolations in each plane.

At any given lattice point, taking appropriate moments of the PDF over velocity space leads to the particle density and velocity. The species particle density n_i is obtained using equation (11) and the total number density n is obtained using equation (12).

$$n_i = f_0^i + f_1^i + f_2^i + f_3^i + f_4^i + f_5^i + f_6^i + f_7^i + f_8^i, \tag{11}$$

$$n = n_1 + n_2 + n_3. \tag{12}$$

If M_i is the molecular weight of species i, the mass density of that species ρ_i and the total mass density ρ are obtained from equations (13) and (14), respectively.

$$\rho_i = M_i n_i, \tag{13}$$

$$\rho = \sum_{i=1}^{3} \rho_i. \tag{14}$$

For species i, the velocity $\boldsymbol{u}_i$ used in the equilibrium function is obtained using equation (15). However, the species velocity $\boldsymbol{u}_i'$ used to compute mole flux is evaluated using equation (16), following Shan and Doolen [9]. For consistency, equation (16) is also used in deriving inflow and outflow boundary conditions. The mole flux $\boldsymbol{J}_i$ and mass-averaged mixture velocity $\boldsymbol{u}$ are calculated using equations (17) and (18), respectively. The velocity of all species at solid obstacles is reset to zero at each time step.

$$n_i \boldsymbol{u}_i = \sum_{\alpha=0}^{8} f_\alpha^i \boldsymbol{e}_\alpha^i, \tag{15}$$

$$4n_i \boldsymbol{u}_i' = \left(4 - \frac{1}{\tau_{ij}} - \frac{1}{\tau_{ik}}\right) \sum_{\alpha=0}^{8} f_\alpha^i \boldsymbol{e}_\alpha^i + \left(\frac{1}{\tau_{ij}} + \frac{1}{\tau_{ik}}\right) \sum_{\alpha=0}^{8} f_\alpha^{i,\mathrm{eq}} \boldsymbol{e}_\alpha^i, \tag{16}$$

$$\boldsymbol{J}_i = n_i \boldsymbol{u}_i', \tag{17}$$

$$\rho \boldsymbol{u} = \rho_1 \boldsymbol{u}_1 + \rho_2 \boldsymbol{u}_2 + \rho_3 \boldsymbol{u}_3. \tag{18}$$

Unlike molecular dynamics, which tracks motions of individual molecules, the LB method tracks the statistical behaviour of a large number of molecules at each lattice point. The velocity in equations (15) and (16) thus represents the average velocity of a large number of molecules of species i. The equilibrium functions $f_\alpha^{i(\mathrm{eq})}$ and $f_\alpha^{i(0)}$ are calculated using equations (19) and (20), respectively.

$$f_\alpha^{i(\mathrm{eq})} = \omega_\alpha n_i \left[1 + \frac{\boldsymbol{e}_\alpha^i \cdot \boldsymbol{u}}{c_{s,i}^2} + \frac{(\boldsymbol{e}_\alpha^i \cdot \boldsymbol{u})^2}{2c_{s,i}^4} - \frac{\boldsymbol{u} \cdot \boldsymbol{u}}{2c_{s,i}^2}\right], \tag{19}$$

$$f_\alpha^{i(0)} = \left[1 + \frac{(\boldsymbol{e}_\alpha^i - \boldsymbol{u}) \cdot (\boldsymbol{u}_i - \boldsymbol{u})}{c_{s,i}^2}\right] f_\alpha^{i(\mathrm{eq})}. \tag{20}$$

For the D2Q9 model, the weight functions ω_α in equation (19) are given by [8]

$$\omega_0 = 4/9, \qquad \omega_1 = \omega_3 = \omega_5 = \omega_7 = 1/9,$$
$$\omega_2 = \omega_4 = \omega_6 = \omega_8 = 1/36. \tag{21}$$

In the DLS model [5], the dimensionless speed of sound c_s is different for each species and these different speeds are given by

$$c_{s,1} = \frac{1}{\sqrt{3}}, \qquad c_{s,2} = \frac{1}{\sqrt{3}}\sqrt{\frac{M_1}{M_2}}, \qquad c_{s,3} = \frac{1}{\sqrt{3}}\sqrt{\frac{M_1}{M_3}}. \tag{22}$$

The collision term Ω_α^i for species i along direction α, appearing in equation (7), consists of three different terms, one describing self-collision and the others describing collision with the other two species, as shown in equation (23).

$$\Omega_\alpha^1 = \Omega_\alpha^{11} + \Omega_\alpha^{12} + \Omega_\alpha^{13},$$
$$\Omega_\alpha^2 = \Omega_\alpha^{21} + \Omega_\alpha^{22} + \Omega_\alpha^{23}, \tag{23}$$
$$\Omega_\alpha^3 = \Omega_\alpha^{31} + \Omega_\alpha^{32} + \Omega_\alpha^{33}.$$

The *self-collision* terms for species 1, 2 and 3 are given by equations (24). These represent collisions between particles of the same species.

$$\Omega_\alpha^{11} = -\left(\frac{f_\alpha^1 - f_\alpha^{1(0)}}{\tau_1}\right), \qquad \Omega_\alpha^{22} = -\left(\frac{f_\alpha^2 - f_\alpha^{2(0)}}{\tau_2}\right),$$
$$\Omega_\alpha^{33} = -\left(\frac{f_\alpha^3 - f_\alpha^{3(0)}}{\tau_3}\right). \tag{24}$$

The *cross-collision* terms given by equation (25) represent the effect of collisions between particles of different species and arise only when there is more than one species and the relative velocity between particles of different species is non-zero. In particular, the cross-collision terms are all zero at lattice points on the surface of solid obstacles.

$$\Omega_\alpha^{ij} = -\frac{1}{\tau_D^{ij}} \left(\frac{\rho_j}{\rho}\right) \frac{f_\alpha^{i(\mathrm{eq})}}{c_{s,i}^2} (\boldsymbol{e}_\alpha^i - \boldsymbol{u}) \cdot (\boldsymbol{u}_i - \boldsymbol{u}_j). \tag{25}$$

Note that there are two sets of relaxation times in this LB scheme. The first set $\{\tau_1, \tau_2, \tau_3\}$ appearing in equation (24) controls the kinematic viscosity ν_i of species i via the relationship $\nu_i = (2\tau_i - 1)/6$. Unless mentioned otherwise, all these have been set to unity in this work ($\tau_1 = \tau_2 = \tau_3 = 1$). The second set $\{\tau_D^{12}, \tau_D^{23}, \tau_D^{31}\}$ appearing in equation (25) controls the inter-species diffusivities via the relation

$$D_{ij} = \frac{\rho P}{n^2 M_i M_j} \left(\tau_D^{ij} - \frac{1}{2}\right). \tag{26}$$

The total pressure P appearing in equation (26) is obtained using

$$P = \rho_1 c_{s,1}^2 + \rho_2 c_{s,2}^2 + \rho_3 c_{s,3}^2. \tag{27}$$

Using equations (22) and (27), it can be shown that

$$P = M_1 n/3. \tag{28}$$

It can be seen from equation (28) that if the total pressure remains constant, the total concentration n also remains constant. This is true even when the molecular weights of diffusing species are different. Substituting equation (28) in (26), it can be shown that for any two species i and j,

$$D_{ij} = \frac{M_1}{M_i M_j}\left[\frac{\rho}{n}\right]\left(\frac{2\tau_D^{ij} - 1}{6}\right). \tag{29}$$

Rearrangement of equation (29) leads to equation (30), which is used in practice to calculate relaxation times at different lattice points, given specified values of the diffusivities.

$$\tau_D^{ij} = \frac{1}{2} + 3D_{ij}\frac{M_i M_j}{M_1}\left[\frac{n}{\rho}\right]. \tag{30}$$

To avoid numerical instability in the LB method, it is recommended that the diffusivity values be scaled up such that the relaxation times are of the order of unity.

3.2. Treatment of concentration and flux boundaries

As shown in figure 1, mole fractions $\{X_1, X_2, X_3\}$ (particle densities) are specified at $x = 0$ and mole flux $\boldsymbol{J}$ (particle velocity) is specified at $x = L$. Unlike traditional CFD methods based on the Navier–Stokes equations, where boundary conditions are directly prescribed on the velocity and density, boundary conditions in the LB model need to be prescribed indirectly using the PDF. In this section, the inflow and outflow conditions on the PDF are derived based on the particle velocity, equation (16). The basic sets of equations needed are equations (11) and (16). Since the base velocities can be different for each species, a modified velocity $\tilde{\boldsymbol{u}}_i' = \boldsymbol{u}_i'\sqrt{\frac{M_i}{M_1}}$ and a relaxation parameter $\phi = \left(\frac{1}{\tau_{ij}} + \frac{1}{\tau_{ik}}\right)$ are defined. Using these definitions, equation (16) can be written as two sets of equations, along the x and z axes and these are given by (subscript i is dropped for clarity)

$$4n\tilde{u}_x' = (4-\phi)(f_1 + f_2 + f_8 - f_4 - f_5 - f_6) + \phi(f_1^{(\mathrm{eq})} + f_2^{(\mathrm{eq})} + f_8^{(\mathrm{eq})} - f_4^{(\mathrm{eq})} - f_5^{(\mathrm{eq})} - f_6^{(\mathrm{eq})}), \tag{31}$$

$$4n\tilde{u}_z' = (4-\phi)(f_2 + f_3 + f_4 - f_6 - f_7 - f_8) + \phi(f_2^{(\mathrm{eq})} + f_3^{(\mathrm{eq})} + f_4^{(\mathrm{eq})} - f_6^{(\mathrm{eq})} - f_7^{(\mathrm{eq})} - f_8^{(\mathrm{eq})}). \tag{32}$$

The last boundary condition needed is equation (11). Based on a treatment similar to that used by Zou and He [10], equations (11), (31) and (32) can be used to determine unknown PDF values at the inlet and outlet. The particle density is specified at $x = 0$ and the x-component of particle velocity is specified at $x = L$. The z-component of velocity is extrapolated from the domain interior at both the concentration ($x = 0$) and flux ($x = L$) boundaries.

Thus, at $x = 0$, the unknown PDF values after streaming (refer to figure 2(*a*)) are $\{f_1, f_2, f_8\}$. The values of equilibrium functions in equations (31) and (32) are calculated from the previous time-step and are thus known quantities. Defining

$$S_1 = f_1^{(\mathrm{eq})} + f_2^{(\mathrm{eq})} + f_8^{(\mathrm{eq})} - f_4^{(\mathrm{eq})} - f_5^{(\mathrm{eq})} - f_6^{(\mathrm{eq})}, \tag{33}$$

$$S_2 = f_2^{(\mathrm{eq})} + f_3^{(\mathrm{eq})} + f_4^{(\mathrm{eq})} - f_6^{(\mathrm{eq})} - f_7^{(\mathrm{eq})} - f_8^{(\mathrm{eq})}, \tag{34}$$

equations (11), (31) and (32) can be rearranged to give

$$f_1 + f_2 + f_8 = n - (f_0 + f_3 + f_4 + f_5 + f_6 + f_7), \tag{35}$$

$$f_1 + f_2 + f_8 = f_4 + f_5 + f_6 + \left[\frac{4n\tilde{u}_x' - \phi S_1}{4-\phi}\right], \tag{36}$$

$$f_2 - f_8 = -f_3 - f_4 + f_6 + f_7 + \left[\frac{4n\tilde{u}_z' - \phi S_2}{4-\phi}\right]. \tag{37}$$

Equating the right-hand side of equations (35) and (36), it is seen that

$$n = \left[(4-\phi)(f_4 + f_5 + f_6) + (4-\phi)(f_0 + f_3 + f_4 + f_5 + f_6 + f_7) - \phi S_1\right]\left[(4-\phi) - 4\tilde{u}_x'\right]^{-1}. \tag{38}$$

If the particle velocity is specified, equation (38) is used to obtain the particle density and vice versa. Next, to obtain f_1, it is assumed that [10] $f_1 - f_1^{\mathrm{eq}} = f_5 - f_5^{\mathrm{eq}}$ and this leads to

$$f_1 = f_5 + \frac{2n\boldsymbol{u}_x}{9C_{s,i}^2}. \tag{39}$$

Note that the velocity component used in equation (39) is the mass-averaged mixture velocity from equation (18). Substituting equation (39) in (36),

$$f_2 + f_8 = f_4 + f_6 + \left[\frac{4n\tilde{u}_x' - \phi S_1}{4-\phi}\right] - \frac{2n\boldsymbol{u}_x}{9C_{s,i}^2}. \tag{40}$$

Equations (37) and (40) can now be solved simultaneously to obtain f_2 and f_8. A similar procedure is followed at the right boundary to determine the unknown values $\{f_4, f_5, f_6\}$. The implementation of these boundary conditions is carried out at each lattice point on the left and right boundaries. However, if an obstacle is present at the boundary, the bounce-back condition is implemented at that lattice point, as discussed in section 3.3. It is found that the stability of the scheme just discussed may improve if the equilibrium terms defined by equations (33) and (34) are calculated using an average value between two successive time steps. Care should be taken when specifying the mole flux of species 2 and 3 and in extrapolating the velocities at the left and right boundaries because the species velocity $\tilde{\boldsymbol{u}}_i'$ is used in boundary condition calculations. When the boundary condition implementation discussed in this section is adapted to the D3Q19 model in 3D, the number of unknown PDFs is found to be more than the number of available equations. In this case, an iterative solution procedure can be used to obtain these unknown PDFs at a given time level.

3.3. Treatment of impermeable obstacles

Obstacles within the flow domain are treated like impermeable solids with zero mass flux in a direction normal to their surface. The zero normal flux condition is usually sufficient for conventional mass transfer models based on the Ficks law of diffusion or the Stefan–Maxwell equations. However, drawing a line between pure diffusion and convection is not so convenient in the LB method because it is based on tracking individual particles (representing a large number of molecules). The LB method makes no conceptual distinction between the transport of a single species flowing/diffusing over an obstacle and multiple species flowing/diffusing in opposite directions over the same obstacle. The only difference is that when there are multiple species, they can impede the motion of each other because of inter-particle collisions. The LB method thus operates at a more fundamental level and provides an opportunity to provide a more rigorous physical interpretation of how particles of each species behave when they encounter a solid wall.

In order to model particle–wall interaction, three different boundary conditions (no-slip, free-slip and diffuse reflection) are tested. In the no-slip interaction, particle populations encountering a wall are reflected back in the direction from which they arrive (bounce-back). For the case of free-slip, particle populations are reflected such that the angle of reflection is the same as the angle of incidence. Finally for the case of diffuse reflection, the particle populations are reflected back with equal probability in all directions. Note that the normal component of particle velocity is reversed for all three cases ensuring that the zero normal flux condition is satisfied. Surprisingly, all these types of interactions give the same result as far as mass transport of the species is concerned. A possible explanation of this is that for low speeds, the main obstacle to transport of any given species tangential to the obstacle wall is not the wall itself, but the species getting transported in the opposite direction. This is what one would expect in the continuum regime where collisions between molecules are much more common than collision of molecules with the wall. Thus, in a counter-diffusion problem, the only significant effect of obstacles is to absorb the normal momentum of particles of all species. Out of the three cases, implementing the no-slip condition is the easiest and furthermore, the bounce-back condition is very easy to implement for complex geometries and it was therefore selected for use in this work.

To implement the condition of zero velocity of all species on the surface of a solid obstacle in the LB model, equations (11) and (15) are used to calculate unknown PDF values by setting $\boldsymbol{u} = \boldsymbol{0}$. These unknown PDF values are calculated for three possible configurations illustrated in figure 2(*c*). The calculation for other configurations is similar and can be obtained using symmetry. For locally flat surfaces like point 1 in figure 2(*c*), the unknown PDF values after streaming are $\{f_4, f_5, f_6\}$ and these are obtained using

$$f_4 = f_8 \qquad f_5 = f_1 \qquad f_6 = f_2. \tag{41}$$

In addition to equation (41), a zero gradient condition is also imposed on the particle number density (of all species) at the obstacle surface along the local normal. For convex corners like point 2 in figure 2(*c*), the PDF value after streaming are obtained using

$$f_3 = f_7 \qquad f_4 = f_8 \qquad f_5 = f_1. \tag{42}$$

The zero concentration gradient condition is not imposed for convex corners. Finally, for concave corners like point 3 in figure 2(*c*), the unknown PDF values after streaming are $\{f_1, f_2, f_3, f_4, f_8\}$ and these are obtained using

$$f_1 = f_5 \qquad f_2 = f_6 \qquad f_3 = f_7, \tag{43}$$

$$f_4 = f_8 = \tfrac{1}{2}\{\rho - [f_0 + f_1 + f_2 + f_3 + f_5 + f_6 + f_7]\}. \tag{44}$$

The density ρ in equation (44) is obtained by extrapolation in the normal direction from the domain interior. Note that the simpler equation (15) for determining species velocity was used to develop expressions for PDF values at obstacles, while the slightly more complex equation (16) was used to obtain PDF values at the left and right boundaries.

3.4. Summary of LB algorithm

Species mole fractions are initially assigned the same values over the entire domain and these are their respective values at $x = 0$. The x-component and z-component of species velocities in the fluid region are initially set to zero. For lattice points that lie on an obstacle boundary, both velocity components are zero at all times. The following six steps are then repeated, in the order shown, for all species simultaneously, until a steady state solution is reached.

1. Calculation of equilibrium functions.
2. Calculation of the collision terms.
3. Streaming and interpolation of PDF values.
4. Calculation of unknown PDF values at $x = 0$ and $x = L$.
5. Calculation of unknown PDF values at obstacle boundaries.
6. Calculation of density, velocity, mole fractions, etc.

As a check, the total concentration is calculated at the end of every calculation in the LB model and it is confirmed that this remains constant at all lattice points irrespective of the numerical parameters used and whether or not obstacles are present in the domain as long as the mass transport occurs in the continuum regime. Conservation of mass is checked by integrating the mole flux of all species along z at $x = 0$ and $x = L$. The numerical parameter space over which solutions can be obtained is restricted by the grid size used, the low Mach number constraint that imposes limits on particle velocities, the low Knudsen number constraint that limits mass transport to the continuum regime and the constraint that binary diffusivity values be large enough to simulate positive inter-diffusion between species.

4. Results and discussion

In most of the results to be discussed, it is found that the species mole flux at $x = 0$ is close to but not exactly equal to the corresponding mole flux for that species at $x = L$ except for some special cases. In addition, it is observed that the mole averaged mixture velocity (and the mole flux of the inert species) in the present LB model is not exactly zero for species

having different molecular weights except at the flux boundary at $x = L$. This discrepancy is thought to arise because the mole flux calculation is based on equation (16), which is an *ad hoc* extension of the earlier approach of Shan and Doolen [9] to three species. In addition, it is important to point out that the present LB method uses a mole based approach, whereas the earlier method development [5,7] (for two species) was a mass based approach.

The LB computations are performed using a SGI Altix supercomputer with 64 GB of configured memory. Numerical solutions to the 1D SM equations are obtained using an Euler integration scheme and numerical solutions to the 2D LE are obtained using an iterative finite-difference procedure. In sections 4.1 and 4.2, the LB model is compared with 1D and 2D solutions to the SM equations, respectively. In section 4.3, more complex geometries are discussed to demonstrate the use of the LB model for such cases.

4.1. One-dimensional mass diffusion

For 1D mass diffusion, solutions of the mole fraction distribution are governed by the dimensionless flux, J^*, defined in equation (45).

$$J^* = JL/(c_T D_{13}). \tag{45}$$

In equation (45), J = mole flux (mol m^{-2} s^{-1}), L = domain length (m), C_T = total molar concentration (mol m^{-3}) and D_{13} = diffusivity between components 1 and 3 (m^2 s^{-1}). Other dimensionless parameters are the diffusivity ratios D_{12}/D_{23} and D_{13}/D_{23}. Comparisons between the LB model and the physical world are made via these dimensionless numbers. The mole flux is constant along the z-axis and there are no obstacles present in the domain.

In order to have a concrete example, calculations are performed for a H_2, H_2O and N_2 system present in the porous anode of a solid oxide fuel cell (SOFC) at ambient temperature (1073 K) and pressure (1 atm). The parameters used are given by: $L = 0.019\,1$ (m), $J = 0.041\,5$ (mol m^{-2} s^{-1}), $c_T = 11.4$ (mol m^{-3}), $D_{12} = 3.37 \times 10^{-4}$ (m^2 s^{-1}), $D_{23} = 0.692 \times 10^{-4}$ (m^2 s^{-1}) and $D_{13} = 1.085 \times 10^{-4}$ (m^2 s^{-1}). Based on equation (45), these values lead to $J^* = 0.64$. A normalized length $x^* = x/L$ is used. At $x^* = 0$, the mole fractions of H_2, H_2O and N_2 are 0.47, 0.03 and 0.5, respectively. As discussed before, the mole flux of H_2 and H_2O at $x^* = 1$ is J and $-J$, respectively. The mole flux of N_2 (inert species) at $x^* = 1$ is zero.

Solutions to the SM equations for these parameters are obtained via numerical integration of equations (3)–(5) using a Euler integration scheme. Direct analytical solutions have also been developed for this case and used to validate solutions obtained via numerical integration. The output of the SM solution is the mole fraction distribution of H_2, H_2O and N_2 from $x^* = 0$ to $x^* = 1$, and for $J^* = 0.64$, the mole fractions of H_2, H_2O and N_2 at $x^* = 1$ are calculated to be 0.0815, 0.5710 and 0.3475, respectively.

Before the LB solution can be obtained, physical parameters need to be converted to LB parameters such that all relevant dimensionless numbers are identical. Note that all LB model parameters are not in physical units, but in an equivalent and consistent system of lattice units. It is found that

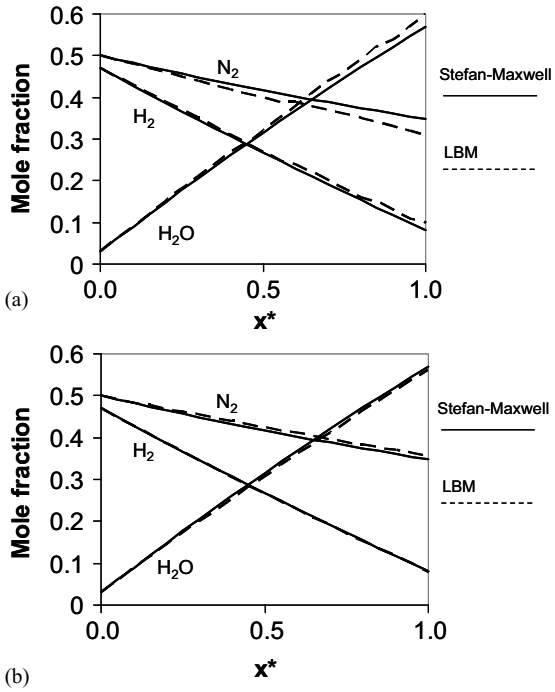

Figure 3. Comparison of LB prediction with the SM solution for $J^* = 0.64$ using actual (*a*) and tuned (*b*) molecular weights. LB parameters (in lattice units): $L = 20$, $J = 0.069$, $c_T = 20$, $D_{12} = 0.337$, $D_{23} = 0.069$ and $D_{31} = 0.1085$.

if diffusivities are too small in the LB model, they can lead to stability problems. This is because the diffusion relaxation times in equation (30) then approach a value of 0.5, which is the limiting value for maintaining positive inter-diffusion coefficients between species. Thus, the LB parameters should be such that diffusivities are in the same ratio as actual diffusivities, but much larger in magnitude. A practical rule of thumb is to ensure that the diffusion relaxation times are unity or greater. Other LB parameters (L, c_T and J) can then be adjusted to maintain the same value of J^*. The particle densities at $x^* = 0$ are set based on known values of mole fractions and total molar concentration. The molecular weights used for H_2, H_2O and N_2 are 2, 18 and 28 (g mol^{-1}), respectively.

A comparison between the predictions of the SM equations and the LB model is shown in figure 3(*a*), where mole fraction variations of H_2, H_2O and N_2 are plotted against the normalized length x^*. As expected, the H_2 mole fraction reduces from $x^* = 0$ to $x^* = 1$ because mass transfer occurs from higher to lower concentrations. Because the H_2 mole fraction at $x^* = 0$ is maintained constant at 0.47, the H_2 mole fraction at $x^* = 1$ depends on the imposed mole flux. A larger mole flux results in lower H_2 mole fraction at $x^* = 1$. The H_2O mole fraction increases as expected from $x^* = 0$ to $x^* = 1$, opposite to the direction of H_2O mole flux. If the mole flux of H_2O increases, the mole fraction of H_2O at $x^* = 1$ increases. Thus, increasing the imposed mole flux leads to larger concentration gradients for both H_2 and H_2O. If J^* is too large, the mole fraction of H_2 at $x^* = 1$ becomes negative in the SM solution. Although valid mathematical solutions are obtained using the SM equations for such cases, negative species mole fractions have no physical meaning. In

the LB simulation, such a case leads to instabilities. For this particular case, the largest permissible value of J^* to avoid negative values is $J^* = 0.78$ and thus a lower value is used. Note that there is no mass transfer of N_2 along the x-axis in spite of the gradient in N_2 mole fraction.

It can be seen from figure 3(*a*) that the prediction of H_2, H_2O and N_2 mole fraction variations using the LB model is close to that obtained from the SM equations, but is not exact. The errors in the mole fraction values at $x^* = 1$ are the least for H_2 and the largest for N_2. A slight oscillation can also be observed in the LB mole fraction profiles in figure 3(*a*), especially for N_2. These errors seem to correspond directly to the molecular weight of the species. When $J^* \ll 1$, the errors between the LB results and SM predictions reduce considerably. In addition, for a system of gases where the molecular weights are not widely different, these errors are small. The system of gases $\{H_2, H_2O, N_2\}$ used in this section has a relatively large variation in molecular weights and represents a somewhat extreme case for the LB model. A comparison of the mole flux at the inlet and outlet shows a difference of about 11.1% for H_2 and 7.6% for H_2O.

An approach to reduce the errors in the LB model by molecular weight tuning will now be discussed. Actual binary diffusivity values are calculated based on the molecular weights of the species involved. However, as the molecular weights of species can be specified independently of the diffusivities between the species in the LB model, it is possible to specify the correct diffusivity values even when the molecular weights do not correspond to the actual gas species. This feature can be used to further improve the accuracy of LB predictions. It is found that the LB predictions are more accurate when the relaxation times controlling inter-component diffusivities are such that $\tau_D^{12} = \tau_D^{23} = \tau_D^{31}$. It can be seen from equation (30) that if molecular weights are adjusted according to equation (46), this objective can be met.

$$\frac{M_1}{M_2} = \frac{D_{23}}{D_{13}}, \qquad \frac{M_1}{M_3} = \frac{D_{32}}{D_{12}}. \tag{46}$$

To illustrate the effect of tuning this ratio, the prior simulation was run again with tuned values of molecular weights ($M_1 = 1$, $M_2 = 1.56$ and $M_3 = 4.91$) and presented in figure 3(*b*). It can be seen that there is a remarkable improvement in the accuracy and LB predictions now exactly match profiles obtained by solving the SM equations. The tuned molecular weights do not vary as much as the original values. In addition, it is found that tuning molecular weights substantially reduces the mole balance error to 4.48×10^{-6}% for H_2 and 3.5% for H_2O.

In general, given any set of diffusivity values, equation (46) can be used to calculate the appropriately tuned molecular weights. Figure 4 plots the percentage error in the N_2 mole fraction at $x^* = 1$ against J^* using actual and tuned molecular weights. Note that the error reduces with reducing J^* even when actual molecular weights are used. Thus, the current model, with actual molecular weights, leads to high accuracy at low J^*. Tuning the molecular weights produces a drastic improvement in accuracy, leading to solutions that are accurate to within 2% across all J^*. For the remainder of this paper, tuned molecular weights are used for three species unless indicated otherwise. The errors at large J^* may be reduced by use of a more accurate interpolation scheme or

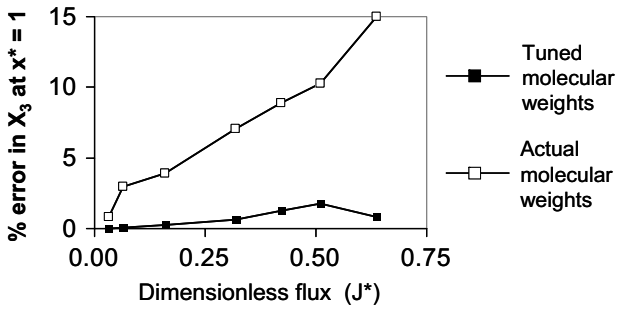

Figure 4. Effect of molecular weight tuning and dimensionless flux (J^*) on the % error in N_2 mole fraction at $x^* = 1$. LB parameters (in lattice units): $L = 20$, $J = 0.069$, $D_{12} = 0.337$, $D_{23} = 0.069$ and $D_{31} = 0.1085$. J^* changed by varying c_T.

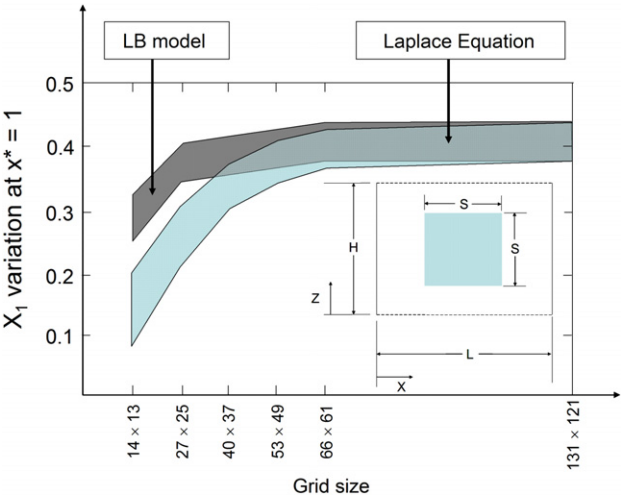

Figure 5. Mole fraction X_1 at $x^* = 1$ for binary diffusion around a square obstacle using different grid sizes in the LB model and using LE for $J^* = 0.125$, $H/L = 12/13$, $\varepsilon = 0.52$ and $X_1 = 0.9$ at $x^* = 0$. LB parameters (in lattice units): $L = \{13|26|39|\ldots\}$, $J = 0.2$, $c_T = \{104|208|312|\ldots\}$ and $D_{12} = 0.2$.

by a more accurate boundary treatment. However, for most mass diffusion problems in porous media, J^* tends to be small and accurate results can be obtained with or without tuning molecular weights. If the molecular weights of diffusing species are identical ($M_1 = M_2 = M_3$), the LB model accuracy improves dramatically. In this case, the diffusivity values are also identical and no interpolation is necessary during the streaming step. It has been verified that the results presented in this section hold true when the underlying LBM model is extended to 3D. However, because the geometrical complexity and computational cost of a 3D simulation is higher by an order of magnitude, only 2D results have been presented in subsequent sections.

4.2. 2D mass diffusion around a square obstacle

To validate the LB model for 2D, a domain of size $L \times H$ with a centrally placed square obstruction of size $S \times S$ is chosen (figure 5 inset) with specified mole fraction $X_1 = 0.9$ at $x^* = 0$ and specified mole flux J at $x^* = 1$. Periodic boundary conditions are imposed at the top and bottom boundaries. The concentration gradient normal to the surface of the square

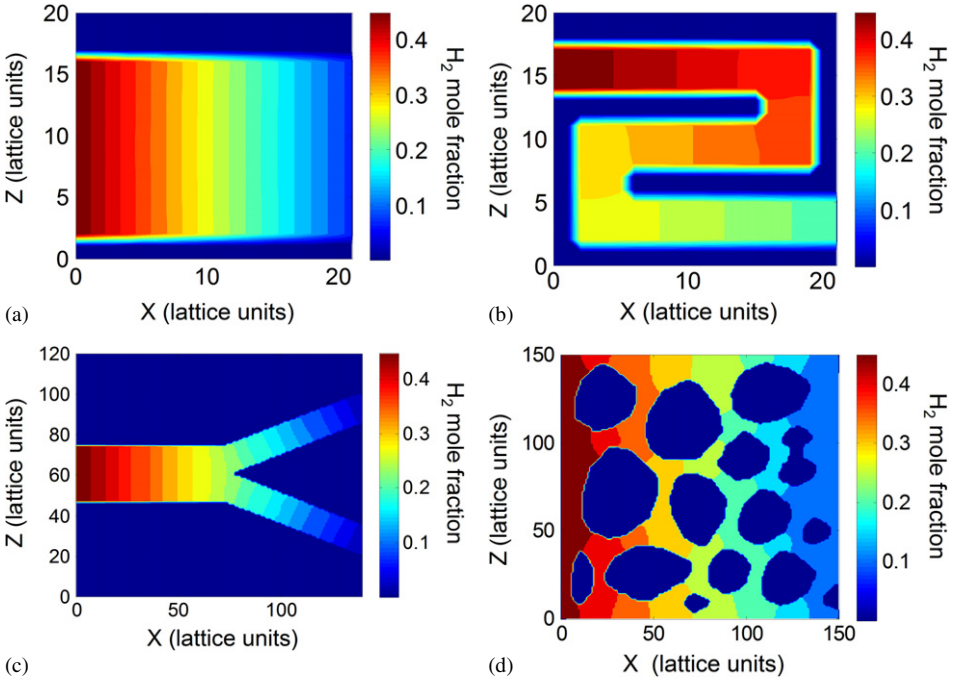

Figure 6. H_2 mole fraction distribution using the LB model for (*a*) straight channel, (*b*) tortuous channel, (*c*) forked channel and (*d*) porous geometry.

obstruction is zero. As before, the solution is governed by the dimensionless flux, $J^* = JL/(c_T D_{12})$. (D_{12} is used in this case because there is no component 3.) Additional parameters for this case are the aspect ratio H/L and the porosity $\varepsilon = 1 - S^2/LH$, which is the ratio of flow area to the total area. The parameter values selected for validation are: $J^* = 0.125$, $H/L = 12/13$ and $\varepsilon = 0.52$. At $x^* = 0$, $X_1 = 0.9$ and at $x^* = 1$, $-c_T D_{12} \partial X_1/\partial x = J$ or $\partial X_1/\partial x^* = -J^*$.

Since there are only two species, the solution to the mole fraction distribution X_1 over the 2D domain can be obtained using $\nabla^2 X_1 = 0$ (equation (6)). Because the flux of component 1 is mainly along x, the mole fraction X_1 gradually reduces from $x^* = 0$ to $x^* = 1$. The distribution $X_1(x, z)$ is symmetric about the horizontal centreline. Because of the square obstacle, X_1 at $x^* = 1$ varies with z and the results are summarized using minimum and maximum values of X_1 at $x^* = 1$. The minimum X_1 at $x^* = 1$ occurs at the centreline, at $z = H/2$, showing that the effect of the square obstacle is maximum at this point. Figure 5 shows the results of the numerical solution for a range of grid sizes, where the band indicates the amount of variation of X_1 at $x^* = 1$. For the coarsest grid (14×13) solution of the LE, X_1 varies from 0.08 to 0.2 at $x^* = 1$. The grid is successively refined until a grid-independent result is obtained. The largest grid size used is 131×121 and for this case, X_1 varies from 0.38 to 0.44, which corresponds to the exact or grid-independent solution.

For comparison, the same lattice sizes used in the numerical solution of the LE are also used in the LB model simulations. For all LB grids, $X_1 = 0.9$ at $x^* = 0$ and $J = 0.2$ at $x^* = 1$. Other parameters used for a 14×13 lattice are: $L = 13$, $c_T = 104$ and $D_{12} = 0.2$, leading to $J^* = 0.125$. For larger grids, the length (in lattice units) increases and c_T is increased by the same factor, keeping J^* constant at 0.125. As an example, for the 27×25 grid, $L = 26$ and $c_T = 208$. The molecular weights are $M_1 = 2$ and $M_2 = 18$. Note that tuning is not required for binary diffusion. Figure 5 plots the LB results for various grid sizes and good agreement with the grid-independent LE solution is found for a sufficiently high lattice resolution. Figure 5 demonstrates that for a given lattice resolution, the LB method gives more accurate results compared with the LE solution. The exact order of accuracy depends on the boundary conditions treatment, and the bounce-back scheme used has been demonstrated to be between first- and second-order accurate [11]. As an additional check, the LB model is used to compute the vector sum $\boldsymbol{J}_1 + \boldsymbol{J}_2$ at all lattice points and this is found to be of the order of 10^{-2} for both coordinate directions for this particular case. If $M_1 = M_2$, it is found that $\boldsymbol{J}_1 + \boldsymbol{J}_2$ is of the order 10^{-8}. The mole balance error for H_2 and H_2O is 12% and 8%, respectively, for the coarse grid (14×13) and reduces to 2.74% and 0.25%, respectively, for a finer grid (66×61). This indicates that conservation of mass in the LB method improves with the grid resolution. Compared with the 1D solution discussed in section 4.1, the maximum permissible J^* (in order to maintain positive H_2 mole fractions at $x^* = 1$) is lower for 2D mass diffusion in the presence of obstacles. Thus, a larger concentration gradient is required to accomplish the same amount of mass transfer when obstructions are present.

4.3. 2D mass diffusion in complex geometries

The previous sections demonstrate that the LB model can give accurate predictions of both 1D and 2D mass diffusion. The LB model is now used to demonstrate three-species mass diffusion in more complex geometries. In general, the SM equations can no longer be easily solved for such cases, and the LB model can serve as a useful predictive tool. Four different geometries in order of increasing complexity are discussed. In figure 6(*a*), diffusion occurs through a straight channel. In figure 6(*b*), diffusion occurs in a tortuous 'S'

shaped channel. In figure 6(*c*) diffusion occurs through a forked channel where a single channel splits into two sub-channels. Finally, in figure 6(*d*) diffusion occurs through a much more complicated geometry typical of porous media. For convenience, the same system of gases (H_2, H_2O, N_2) and hence the same diffusivity values as in section 4.1 have been used. At $x^* = 0$, the mole fractions of H_2, H_2O, N_2 are 0.47, 0.03 and 0.5, respectively, for all cases. Table 1 lists the LB model parameters (in lattice units) used for the different geometries and also lists the percentage error in molar balance at the left and right boundaries for H_2 and H_2O. The results for all cases are discussed in terms of the steady-state H_2 mole fraction profiles. H_2O diffusion roughly occurs in the opposite direction to that of H_2, while N_2 mole fraction reduces in general from $x = 0$ to $x = L$ even if N_2 transport is zero, similar to the 1D solutions discussed in section 4.1.

Consider first the straight channel with impermeable walls. Figure 6(*a*) shows contours of H_2 mole fraction, and mass transport of H_2 occurs in a direction perpendicular to these contour lines, from higher to lower concentration. Because the contour lines are perpendicular to the channel walls, mass diffusion is parallel to the walls and along the x-axis. In fact, it is found that if the separation between the walls is not too small, the walls have an almost negligible effect on mass diffusion and they are similar to insulated walls in a heat conduction problem. This result is therefore almost identical to the 1D result discussed in section 4.1 and good agreement with the 1D SM solution is found with errors of less than 2.7%. The mole balance error between the left and right boundaries of the channel for H_2 and H_2O is 0.25% and 3.3%, respectively, and these errors reduce further as the separation between the channel walls is increased. The channel width along z has a very slight effect on the mass diffusion in the continuum regime. This behaviour is in contrast to the advective flow of a single fluid through a confined channel where walls have a marked effect on the velocity profiles and the shear stress introduces resistance to fluid flow. No such resistance is encountered for pure mass diffusion even if the no-slip velocity boundary conditions are applied at channel walls. Exceptions to this can occur when there is generation or consumption of species at the wall surface due to adsorption, desorption or chemical reactions or if diffusion occurs in the non-continuum regime. Adding to these additional effects is part of ongoing work and results will be reported in a future publication.

Consider next the tortuous channel of figure 6(*b*). Like the straight channel, it can be observed from figure 6(*b*) that there are no gradients of H_2 mole fraction normal to the channel surfaces. Thus, mass diffusion of H_2 again occurs parallel to the channel walls. However, because of the tortuosity of the path, the gas has to diffuse over a longer length, creating an increased resistance to mass transfer. This causes the H_2 mole fraction at $x^* = 1$ to be considerably lower than a corresponding straight channel. A lower value of $J^* = 0.16$ is therefore used to maintain a positive H_2 mole fraction at $x^* = 1$. The actual (tortuous) length, measured along the channel centreline over which diffusion occurs is $L' = 61$ lattice units. As expected, it is found that the 2D solution compares well with the 1D SM solution for the same set of parameters with a longer length $L' = 61$. In this case, the medium tortuosity $\Im$ is defined as the ratio L'/L. The concept of tortuosity is intuitively easy to understand for this simple case, but for more complex geometries, it is difficult to isolate and calculate $\Im$ in this manner because diffusion pathways can branch and re-connect in complex ways. From table 1, it can be observed that the mole balance error for the tortuous channel is 0.86% for H_2 and 2.9% for H_2O. These errors reduce when the grid resolution is increased.

Table 1. LB model parameters for different geometries.

Parameters	Straight channel	Tortuous channel	Forked channel	Porous medium
Grid size	22 × 21	22 × 21	141 × 121	151 × 151
L	21	21	140	150
J	0.069	0.069	0.069	0.069
c_T	21	84	140	600
D_{12}	0.337	0.337	0.337	0.337
D_{23}	0.069	0.069	0.069	0.069
D_{31}	0.108	0.108	0.108	0.108
J^*	0.64	0.16	0.64	0.16
% Error (H_2 mole balance)	0.25	0.86	0.9	3.4
% Error (H_2O mole balance)	3.31	2.9	2.7	2.1

To take the simplest example of path branching, consider the forked channel of figure 6(*c*). The geometry is designed such that the combined width of the two sub-channels is the same as the width of the parent channel. Figure 6(*c*) shows that the H_2 mole fraction reduces from $x^* = 0$ to $x^* = 1$, as expected. The H_2 mole fraction distribution in the sub-channels is also symmetric because the channel widths and branching angles are symmetric. However, it is found that the H_2 mole fraction at the end of the forked channels (at $x^* = 1$) is lower compared with results for a straight channel shown in figure 6(*a*), even when all dimensionless parameters are identical. This observation can once again be explained based on the concept of tortuosity. It can be seen that for part of the forked channel, the gas in the two sub-channels has to diffuse along a diagonal direction, which is larger in length compared with the corresponding horizontal direction along x. The larger the branching angle, the larger will be this length difference. Thus, a larger H_2 concentration drop occurs for the same H_2 mole flux. Both in this case and the previous case of a single 'S' shaped path, the diffusion coefficients D_{ij} can be modified using the channel tortuosity to obtain a so-called effective diffusion coefficient D_{ij}^{eff}, defined such that $D_{ij}^{\text{eff}} = D_{ij}/\Im$. In this case, the actual domain length L is retained, and the effect of longer paths is accounted for by using D_{ij}^{eff} in all the calculations. The mole balance errors for H_2 and H_2O are 0.9% and 2.7%, respectively.

Finally, consider the geometry shown in figure 6(*d*), designed to resemble a porous medium. This geometry provides an example of where there is no intuitive or easy way to calculate tortuosity. In some applications, the porous geometry can be obtained by electron microscope images, converted to digital form and used as an input to the LB model. Based on the currently available computational resources, the resolution adopted for this case is such that there are at least 4 or 5 lattice points in the flow passages between obstacles. As expected, figure 6(*d*) shows that the mole fraction of H_2

reduces in general from $x^* = 0$ to $x^* = 1$. The mole fraction contours can be seen to intersect the solid obstacles normal to the surface, indicating that mass diffusion of H_2 occurs parallel to the obstacle surface. If non-continuum effects are ignored, low porosity leads to a higher resistance to mass diffusion because flow paths become more and more tortuous. Although not apparent in figure 6(*d*), the H_2 mole fraction varies with z at $x^* = 1$ and the lowest H_2 mole fractions are usually found close to solid obstacles, much like the result for the square obstacle in section 4.2. The mole balance errors for H_2 and H_2O are 3.4% and 2.1%. These errors can be reduced further by increasing the lattice resolution.

Note that the tortuosity factor for a given geometry can be calculated if required. For example, in figure 6(*d*), the average H_2 concentration at $x^* = 1$ from the LB model is found to be 0.1. Using the 1D SM solution procedure from section 2, it can be found by trial and error that a similar H_2 mole fraction can be achieved for a geometry without obstructions when D_{ij} are all reduced by a factor of 3.8, implying that $\Im = 3.8$ for the porous geometry of figure 6(*d*). Numerical experiments using the LB model can be carried out to establish tortuosity factors for arbitrary geometries for use in simplified, 1D mass transport models. However, 1D models cannot be used for optimization of the porous geometry. The LB model is able to calculate detailed mass transfer through a porous medium without any empirical modifications to the binary diffusivity values.

5. Conclusion

LB models have developed to the point where continuum, multi-component mass diffusion through complex geometries can be simulated accurately. This work is part of an ongoing development to employ LB models for modelling multi-component gas diffusion through porous media. The two main contributions of this work are enhanced boundary treatment for the multi-component LB model based on average particle velocity and a validation of the LB model against the solutions to the SM equations. One- and two-dimensional tests for three species indicate that the LB model developed in this study can be used for more complex geometries provided a sufficiently high resolution lattice is used. Examples of mass transport through complex geometries illustrate the effect of medium tortuosity. While tortuosity provides an intuitive understanding of mass transport through complex geometries, it is not required as a parameter for LB calculations. Numerical experiments using the LB model can be carried out to establish tortuosity factors for arbitrary geometries for use in simplified, 1D mass transport models. However, 1D models cannot be used for the optimization of the porous geometry. The LB model is able to calculate detailed mass transfer through a porous medium without any empirical modifications to the binary diffusivity values. The effect of porous geometry on mass transfer can thus be directly probed.

Ongoing efforts in this direction include broadening the range of application of this multi-component LB model to non-continuum flow regimes so that high Knudsen number diffusion can be modelled and to include adsorption and chemical reaction dynamics at wall surfaces. Additional work to improve the accuracy of the proposed method for high J^* is also worth pursuing. When used in conjunction with advanced 3D imaging techniques, extensions of the current model to 3D will provide a very powerful tool for the analysis of multi-component mass transport problems through real world geometries. One such application related to solid oxide fuel cell electrodes is reported in [12].

Acknowledgments

Financial support from the Army Research Office Young Investigator Program is gratefully acknowledged. Computational resources were provided by the Booth Engineering Center for Advanced Technologies (BECAT) at the University of Connecticut.

References

[1] Jiang Yi and Virkar A V 2003 *J. Electrochem. Soc.* **150** A942
[2] Ilter M, Ozilgen M and Orbey N 1991 *Polym. Int.* **25** 211
[3] Chau J F, Or D and Sukop M C 2005 *Water Resources Res.* **41** W08410
[4] Chen S and Doolen G D 1998 *Ann. Rev. Fluid Mech.* **30** 329
[5] McCracken M E and Abraham J 2005 *Phys. Rev.* E **71** 046704
[6] Bird R B, Stewart W E and Lightfoot E N 2002 *Transport Phenomenon* (New York: Wiley)
[7] Luo L S and Girimaji S S 2003 *Phys. Rev.* E **67** 036302
[8] Qian Y H, D'Humieres D and Lallemand P 1986 *Phys. Rev. Lett.* **56** 1505
[9] Shan X and Doolen G D 1996 *Phys. Rev.* E **54** 3614
[10] Zou Q and He X 1997 *Phys. Fluids* **9** 1591
[11] Lai Y G, Lin C-L and Huang J 2001 *Numer. Heat Transfer* B **39** 21
[12] Joshi A S, Grew K N, Peracchio A A and Chiu W K S 2007 *J. Power Sources* **164** 631